Revision 2

Cathodoluminescence properties of quartz eyes from porphyry-type deposits: implications for the origin of quartz

O.V. Vasyukova[1] , K. Goemann[2], V.S. Kamenetsky[1], C.M. MacRae[3] and N.C. Wilson[3]

[1]CODES, University of Tasmania, Hobart 7001, Australia, olgav@utas.edu.au

[2]Central Science Laboratory, University of Tasmania, Hobart 7001, Australia, karsten.goemann@utas.edu.au

[3]Microbeam Laboratory, CSIRO Process Science and Engineering, Clayton, Victoria 3168, Australia, colin.macrae@csiro.au & nick.wilson@csiro.au

Abstract

Hyperspectral cathodoluminescence (CL) mapping combined with electron probe microanalysis (EPMA) and Fourier transform infrared spectroscopy were used for the reconstruction of crystallization conditions of quartz from porphyry environments. Quartz eyes from the two porphyry deposits Rio Blanco (Chile) and Climax (USA) were studied. Three peaks are found to be responsible for the total CL emission: 1.93 eV, 2.05 eV and 2.72 eV. The first two peaks are assigned to O-M (with M being an alkali ion) and oxygen vacancies, respectively. The 2.72 eV peak shows a linear correlation with the Ti concentration determined by EPMA point measurements. In addition, a negative correlation between the 1.93 eV emission and the Al concentration was observed.

Quartz grains often form clusters in which adjacent grains show identical CL patterns, indicating that they crystallized attached to each other and were not disturbed later. Quartz cores display sector zoning and enrichment in Li, OH and sometimes Al, which points to rapid

crystallization from an extremely evolved melt. Quartz rims show high Ti, and low Li and OH content indicating crystallization from a less evolved melt either at higher temperatures or at higher titanium activities. The Al and Ti distribution patterns are frequently not correlated and both show uneven distribution indicating fast growth from inhomogeneous melts. Only Ti displays sharp transitions and fine oscillatory zoning, which can be explained by the higher mobility of Al in the quartz lattice.

The quartz eyes crystallized after magma emplacement under non-equilibrium conditions. It is likely that the crystallization occurred from the melt enriched in Al, Li and OH and probably other metals and/or volatiles on the brink of fluid exsolution. Subsequent fluid exsolution brought about disequilibrium to the system, resulting in dissolution of quartz and redistribution of elements between the melt and the fluid. OH, Li and other alkali metals and volatiles partitioned into the fluid, whereas Ti and Al remained in the melt. Resorption of quartz caused by the fluid exsolution continued until equilibrium was reached again, after which crystallization of quartz rims began from the water-, alkali- and volatile-poor melt with higher Ti activity. Further accumulation of Al and Ti in the residual melt led to crystallization of extremely Al- and Ti-rich quartz.

Keywords: cathodoluminescence of quartz, trace elements, lattice defects, porphyry-type deposits

Introduction

Cathodoluminescence (CL), the emission of light resulting from electron bombardment, has proven to be an excellent tool in visualizing intra-granular primary (growth) and secondary (fractures, halos of secondary quartz around fluid inclusions, etc.) textures in quartz. Crystal defects like vacancies and impurities create additional states with distinct energies in the band gap between electron valence and conduction band, leading to the emission and absorption of CL bands with characteristic wavelengths. Internal structure becomes visible due to different

trace element and crystal lattice defects (Götze, 2009; Müller, 2000; Stevens-Kalceff, 2009). Changes in the quantity and quality of defects and impurities in quartz reflect changes of physico-chemical conditions of crystal growth. CL is being used successfully for reconstructions of growth history of quartz and crystallization conditions (Allan and Yardley, 2007; D'Lemos et al., 1997; Monecke et al., 2002; Müller, 2000; Penniston-Dorland, 2001; Peppard et al., 2001; Wark et al., 2007).

The cathodoluminescence spectrum consists of intrinsic and extrinsic contributions. Intrinsic luminescence characterizes the host lattice (Si–O framework) and is caused by non-stoichiometry (vacancies) or structural imperfections (poor ordering, radiation damage, shock damage), which distort the crystal lattice and larger defects such as dislocations and clusters.

Extrinsic luminescence results from impurities often referred to as activators (Müller, 2000). Typical substitutes for Si^{4+} in quartz are Al^{3+}, Ti^{4+}, Fe^{3+}, Ge^{4+}, P^{5+}, and Ga^{3+} (Götze, 2009; Müller, 2000). Large open channels in the quartz structure parallel to the c-axis offer locations for interstitial cations such as H^{+}, Na^{+}, K^{+}, Li^{+}, Fe^{2+}, Cu^{+}, Co^{2+}, Ag^{+} (Müller, 2000). Water bound in the quartz lattice is also very important and can be incorporated as OH^{-} linked with Si or as $4H^{+}$ substituting Si^{4+}. Hydrogen and hydroxyl may act as a charge compensator for Al^{3+} (Müller, 2000). Thus Al content might influence the solubility of water in the quartz lattice.

A number of publications on quartz report correlations between trace element impurities and total CL intensity and sometimes also wavelength of CL emission (Allan and Yardley, 2007; Perny and Eberhardt, 1992; Rusk and Reed, 2002; Rusk et al., 2008; Sprunt, 1981; Watt et al., 1997). In quartz the Ti concentration is generally positively correlated with the total CL intensity (Rusk et al., 2008) and Ti impurities cause blue luminescence (Sprunt, 1981).

However, the published data on the influence of aluminum on the total CL intensity is contradictory. Peppard et al. (2001) and Sprunt (1981) found no correlation between Al concentration and total CL intensity. In contrast, Perny and Eberhardt (1992) and Watt et al. (1997) observed a strong positive correlation between Al concentration and total CL intensity.

Rusk et al. (2008) concluded that high temperature quartz shows a positive correlation between Al and CL intensity, whereas there is a negative correlation in low temperature quartz. Ramseyer and Mullis (1990) showed that Al-rich zones are associated with blue luminescence, but the luminescence intensity in these zones is not correlated with Al concentrations. Hence, if Al is correlated with a specific CL band it will not necessarily show correlation with the total CL emission.

Several spectral cathodoluminescence studies of quartz have been carried out to correlate emission bands and trace element impurities (Alonso et al., 1983; Demars et al., 1996; Gorton et al., 1997; Götze et al., 2005; Luff and Townsend, 1990; Müller, 2000). However, these studies did not show any uniform correlation between particular trace elements and CL bands. For example, Ti was found to be associated with 2.6-2.8 eV and with 2.96 eV bands in different studies (Müller, 2000; Sprunt, 1981), and Al was assigned to 2.64, 2.79, 2.9, 3.2 and 3.7 eV bands (Alonso et al., 1983; Demars et al., 1996; Gorton et al., 1997; Luff and Townsend, 1990; Müller, 2000; Nassau and Prescott, 1975; Yang et al., 1994).

In this study we applied hyperspectral CL mapping to quartz grains from porphyry environments to determine the origin of quartz. The term ‘quartz eyes’ is used in preference to other terms (e.g. phenocrysts) to emphasize that their origin is yet to be established. Hyperspectral CL mapping allowed us to extract a set of spectral signatures giving rise to the total CL emission, and together with electron probe microanalysis (EPMA) we were able to assign CL peaks to impurities. Distribution patterns for different CL contributors within quartz eyes were studied. This allows us to make several general conclusions on the origin of quartz eyes.

Samples and Localities

This study focused on three samples. One of them is from a biotite bearing porphyritic granite intrusion which hosts Mo mineralization (Climax porphyry molybdenum mine, central Colorado, USA, sample 109647). The other two samples are porphyritic granites from the Don Luis Porphyry, a post-mineral intrusion within the Los Bronces-Rio Blanco Cu-Mo breccia/porphyry copper deposits in central Chile (samples DC-DP-1 and DC-DLP-1), where mineralization is present, but is generally sub-economic. The samples contain between five and ten percent of quartz eyes, ranging in diameter from 0.5 to 5 mm, and their shapes vary significantly within a single thin section (Table 1). The quartz grains often cluster together with clusters consisting of two to five or more quartz grains. When examined optically in crossed polars, several distinct optical orientations are commonly observed.

A number of quartz eyes were studied from each sample (Table 1) by a combination of optical microscopy, electron probe microanalysis, and backscattered electron (BSE) and panchromatic CL imaging. Three quartz grain clusters were subsequently chosen for further study by hyperspectral CL mapping: Cluster C from sample 109647 (Climax), R1 from sample DC-DP-1, and R2 from DC-DLP-1 (Rio Blanco).

Techniques

Spectral Cathodoluminescence

Cathodoluminescence spectra and hyperspectral maps were collected using the JEOL field emission gun electron microprobe analyzer (JXA 8500F) at CSIRO Process Science and Engineering, Clayton. It is customized with quartz optics, and equipped with an Ocean Optics QE65000 grating Charge Coupled Detector (CCD) spectrometer (MacRae et al., 2005). The spectrometer employs a Hamamatsu S7031-1006 back-thinned CCD and was operated with the

Peltier cooling set at -15°C. A 300 µm diameter optical fiber was used to connect the spectrometer to the collection optics within the microprobe and the diameter of this fiber formed the entrance slit of the spectrometer. This resulted in a spectral resolution of 10.0 nm. Spectra were collected with 1024 equal wavelength windows over the full spectrometer range of 199 to 998 nm. Spectra were not corrected for either detector efficiency or instrumental response. This means that the CL peak calibration is not transferrable to another instrument. All spectra are displayed in energy rather than wavelength as the CL peaks are symmetric in energy space and can be fitted using a series of Gaussian curves.

Hyperspectral CL maps of the quartz samples were collected with an accelerating voltage of 20 kV, beam current of 40 nA, dwell time of 40 ms, with the beam defocused to 2 µm matching the step size of 2 µm in X and Y. Under these conditions the CL yield was linear with titanium concentration indicating the electron beam power density was below the level required to induce damage within the quartz and thus the CL was stable at each pixel. Stage scanning was used to step the sample beneath a fixed beam and maps of up to 1000 by 1500 pixels were collected. For each pixel a full 1024 channel CL spectrum was stored in parallel with WDS measurements of Ti, Al, Fe, and Si to identify the bulk mineralogy and elevated Ti levels.

To identify lines for quantification, both selected area and sum spectra from the map were examined. Peaks were identified and compared to known lines in quartz using a luminescence database (MacRae and Wilson, 2007). Peak deconvolution using three principal Gaussian peaks centered at 1.93 eV, 2.05 eV and 2.72 eV resulted in the lowest residual. Fitting and quantifying was carried out according the procedure of Leeman et al. (2008). Chimage software (Harrowfield et al., 1993) was then used to fit the series of Gaussian curves, in energy space, to the spectrum from each pixel within the CL map, with the peak positions and widths of the Gaussian curves being kept constant, and only the heights of the Gaussian curves being allowed to vary during the least squares fitting.

Electron Probe Microanalysis

To calibrate the fitted 2.72 eV peak intensity against the Ti level, a series of point analyses were performed across the mapped region on the same JEOL electron microprobe used for the spectral CL mapping. The point analyses were performed after the CL mapping, as the long acquisition times associated with trace element point analyses damage the quartz structure and lead to variable CL yields primarily associated with damage. The electron microprobe was operated with an accelerating voltage of 20 kV, a beam current of 200 nA and the beam was defocused to 20 μm. To improve the detection limits on Ti two spectrometers with PET crystals were operated in parallel. Total peak acquisition time on titanium, per spectrometer, was 80 seconds on the peak and 40 seconds on each of the backgrounds, the three sigma detection limit for titanium being 10 ppm (Ancey et al., 1978). To determine the titanium offset caused by slight variations in the x-ray background, a synthetic quartz sample was analyzed. This gave an offset of 8 ppm, which is negligible compared to the Ti levels measured.

A series of points in each of the three samples were analyzed and the measured Ti elemental levels were compared to the fitted peak height of the 2.72 eV line. A series of 20 μm regions equivalent to those analyzed by point analysis were selected from the fitted 2.72 eV data and averaged. The Data for sample 109647 from Climax is presented in Figure 1. It shows a good correlation between peak intensity and Ti concentration. A least squares linear fit of the data gives a calibration curve with an R^2 value of a 0.9631. Errors in the microanalysis are shown in Figure 1 and are typically ±12 ppm.

The JEOL electron microprobe was also used to collect BSE images in parallel to the x-ray and CL mapping. The backscattered electron images show major structures within the quartz eyes but do not reveal the fine detail or zoning visible by means of CL.

Further Ti, Al, and Fe trace element data were obtained on the Cameca SX100 electron microprobe at University of Tasmania using simple oxide standards for calibration, an

accelerating voltage of 15 kV, a beam current of 200 nA, a beam diameter of 5 µm, and counting times of 300 seconds on the peak and 150 seconds on two backgrounds. No significant changes of peak or background intensities during the measurement could be observed, and comparative measurements at shorter acquisition times, lower beam current and higher beam diameter of quartz areas with higher trace element contents yielded similar results. One LPET crystal was used for Ti, two TAP crystals for Al, and two LLiF crystals for Fe, yielding three sigma values for detection limit and analytical precision of 12, 7, and 19 ppm, respectively. Spectrosil 1000 (Saint-Gobain), a fused silica material with certified contents of <20 ppb for Al and <10 ppb for other trace elements, was used to determine blank corrections of +15 ppm for Ti, –26 ppm for Al, and –5 ppm for Fe. Quartz from Hot Springs, Harvard standard 122838 (McGuire et al., 1992), was analyzed with the samples. Trace element data for this standard have not been published, but for comparison values of 1.21 ± 0.01 ppm for Ti, 53 ± 9 ppm for Al, and <3 ppm for Fe were obtained by laser ablation inductively coupled mass spectrometry (LA-ICP-MS) at University of Tasmania. The EPMA results of 1 ppm for Ti, 41 ppm for Al, and 5 ppm for Fe, even though Ti and Fe are below the detection limit, are in reasonable agreement with the LA-ICP-MS data and indicate the blank correction works correctly. Where possible, three EPMA spots were positioned next to each other in bands with similar panchromatic CL intensity to improve counting statistics.

Infrared Spectroscopy

Fourier transform infra-red (FT-IR) spectra of quartz were obtained using a Bruker Vertex 70 system equipped with a Bruker Hyperion 2000 microscope at University of Tasmania. FT-IR spectroscopy was used for the determination of the distribution and specification of structural water in quartz crystals. The analyses were carried out on doubly polished wafers 150 µm in thickness which were cleaned with acetone and dried prior to analysis. The spectra were

acquired in transmission mode with 128 scans, a wave number range of 4000 to 2000 cm^{-1}, and a resolution of 4 cm^{-1}. FT-IR mapping was carried out with the 25 µm aperture and an increment of 25 µm. Background spectra were taken before and after each map. Baseline correction, sample thickness correction and conversion of the transmission spectrum to the absorption spectrum was carried out using the Bruker OPUS software package.

Results

Hyperspectral cathodoluminescence mapping

Three principal contributors were found to be responsible for the total emission: the peaks centered at 1.93 eV, 2.05 eV and 2.72 eV (Fig 2). In the quartz cores (zones I, III and VI, Fig 2) 1.93 eV emission shows higher intensity than the other two emissions. The rims (zones II, V and VII, Fig 2b) are mostly characterized by a dominating 2.72 eV peak, which is especially distinct in zone V within cluster R2 (Fig 2). The 2.05 eV peak is less pronounced than the other peaks and was never found dominating. The major characteristics of the distribution of the intensities corresponding to every peak are described below.

2.72 eV CL emission and corresponding Ti content

Quartz cluster R1 is comprised of two grains, which have almost identical 2.72 eV intensity patterns (Fig 3a). Emission is higher in the rim (zone II in Fig 2a) than in the core (zone I in Fig 2a) with the highest intensity close to the core boundary and the lowest intensity in the inner core. The boundary between core and rim is sharp with no gradational transitions. The core has subtle oscillatory layers but clearly shows sector zoning. There is only one healed fracture visible in the grain which shows a low 2.72 eV intensity.

The quartz cluster R2 (Fig 4a) also contains two grains. The smaller one shows low overall 2.72 eV intensity and has a core (zone III in Fig 2b) with very low emission. The larger grain

consists of two regions with very different intensities and a sharp transition between them. Some weak oscillatory banding can be observed in the lower intensity region (zone IV). The inner part of the high intensity region (zone V) has an irregular pattern resembling sector zoning; its outer part shows euhedral oscillatory zones. There are a number of healed fractures distributed within the grain, which all show low 2.72 eV band intensity. Most of the fractures are localized in the core (zone III) of the small grain (Fig 4a).

The quartz cluster C consists of six individual grains, each showing an internal texture similar to R1 (Fig 5a): a dark inner core (zone VI) and a bright rim (zone VII). Oscillatory zoning occurs in both rims and cores and is more pronounced in the cores compared to R1. All core-rim transitions are sharp, but in general there is more variation in intensity compared to R1. There is a number of healed fractures and star-like patches of secondary quartz with low 2.72 eV intensity.

All the samples showed strong correlation between the 2.72 eV intensity and the Ti content. Figure 1 demonstrates a calibration curve (2.72 eV vs. Ti content) for the cluster C with an R^2=0.9631. Based on this correlation 2.72 eV maps can be converted to Ti distribution maps and the following general observations can be made. The Ti concentration is higher in rims than in cores (C and R1) or in particular outer zones (R2). Actual Ti concentrations for every grain are shown in Figures 3d, 4d and 5d; ranges of Ti concentrations within the different zones of the clusters are shown in Table 2. Adjacent grains within a cluster can vary significantly in Ti content, e.g. in C two adjacent grains within the cluster have Ti concentration almost twice as high as the other grains (Fig 5a, zones VIIa and VIIb). The Ti content changes abruptly at transitions between rim and core which are only a few micrometers wide.

1.93 eV CL emission, correlation with 2.72 eV emission and Ti and Al content

The distribution pattern of the 1.93 eV emission intensity within R1 is different from the 2.72 eV emission (compare Figs 3a and b). 1.93 eV emission is high in the rim and the outer

core, and very weak in the inner core and along the core-rim transition. In the inner core sector zoning is observed. Low 1.93 eV intensities within these sectors correlate with high 2.72 eV intensities (higher Ti concentrations), but there are patches of extremely high 1.93 eV intensity within the inner core not corresponding to low 2.72 eV intensities. The core-rim transition is sharp along some faces and diffusional along the others. The fracture shows high 1.93 eV intensity.

The two grains in R2 behave differently (Fig 4b). The 1.93 eV map of the larger grain is almost a negative image of the 2.72 eV distribution, whereas the smaller grain shows lower 1.93 eV intensity in the core and higher intensity in the rim, as is the case for 2.72 eV. There are numerous healed fractures within the grain which vary in 1.93 eV band intensity; some of them are not visible in the 2.72 eV band map. Most of the fractures are localized in the core of the small grain (Fig 4b).

Within C, the main characteristics of the 1.93 eV emission inversely correlate to 2.72 eV (Fig 5b), but show less oscillatory zoning in the rim and a marble-like texture overall (Fig 6c) due to numerous irregular fractures, which are not visible in the 2.72 eV map. Transitions between cores and rims are diffusional. The healed fractures and star-like patches also visible in the 2.72 eV map show very high 1.93 eV intensity. The marble-like texture does not correlate with fluid inclusion trails.

To investigate further correlation between trace element concentrations and CL emission, additional electron microprobe point analyses were performed and superimposed onto the CL maps. Generally, Al concentration in the samples ranges from around 100 to 150 ppm (Figs 3d, 4d and 5d) with rare spikes (as in the sample C, Figs 5d and 6e); only in the sample R2 two zones (III and V) showed extreme enrichment in Al content (from about 900 to 4000 ppm, Fig 4d).

All the samples showed strong negative correlation between the 1.93 eV intensity and the Al concentrations (Figs 3d, 4d, 5d and 6). Figure 6d demonstrates a linear fit between 1.93 eV

intensity and Al content with R^2 = 0.8558 for cluster C. The spike of 336 ppm in the Al profile in Fig 6a is related to an Al-rich inclusion (see insert 1 in Fig 6e). Although the optical image of the spot after EPMA does not show an inclusion (insert 2 in Fig 6e) for the spike of 173 ppm, it still can be related to a microinclusion which is too small to be seen with the optical microscope. Therefore these two spikes were excluded from the plot in Fig 6d. Grains R1 and R2 showed similar negative correlation between the 1.93 eV intensity and Al content with the exception of the upper zone of the bigger grain in R2, where concentrations of both Al and Ti are extremely high.

2.05 eV CL emission

The fitted 2.05 eV emission map for R1 shows a sharp transition between rim and outer core and a diffusive transition between outer and inner core similar to the 1.93 eV map with the intensity decreasing from rim to inner core (Fig 3c). For clusters R2 and C, the 2.05 eV distribution patterns are also quite similar to the 1.93 eV maps, but show more diffusional transitions (Figs 4c and 5c).

Transmitted light

In transmitted light the quartz eyes are homogeneous. The clusters R1 and C contain small feldspar inclusions. No melt inclusions were found in the samples. All quartz grains contain secondary aqueous inclusions localized along healed fractures, which are visible in the 2.72 eV and sometimes in the 1.93 eV emission maps (Fig 7a-c). The only exception is zone V in cluster R2 (Fig 7d-f). It contains abundant very small fluid inclusions (1-2 μm), but does not display many healed fractures, which may indicate a primary origin of the inclusions. The largest fluid inclusions contain a gas bubble and often a daughter crystal. Inclusions from these particular quartz grains were not studied in detail, but in other samples from Rio Blanco aqueous inclusions showed heterogeneous compositions from vapor-rich varieties to brines (Vasyukova,

2011). Such inclusion assemblages are common in porphyry-related environments (Roedder, 1984; Wilkinson, 2001).

Infrared spectroscopy

Five absorption bands were observed in the IR spectra within cluster R1 which are centered at 3482, 3425, 3378, 3317 and 3205 cm^{-1} (Fig 8a). The 3378 cm^{-1} peak is the most intensive; its distribution map shows higher absorption in the inner core of the grain and lower absorption in the rim zone (Fig 8d). The 3482 cm^{-1} peak is less intensive and demonstrates a similar pattern, i.e. higher intensity in the core than in the rim (Fig 8c). Intensities of both absorption bands are negatively correlated with the 1.93 eV CL emission, which shows higher intensity in the rim than in the core (Fig 8b). Bands at 3425, 3317 and 3205 cm^{-1} show very low intensity and no distinct distribution patterns.

Discussion

Attribution to point defects

Two major CL emission bands are generally the principal contributors to the CL emission of igneous and metamorphic quartz with maxima at ~2.7 eV and ~1.9 eV, and the total CL emission depends on the relative intensities of these two dominant emission bands (Götze et al., 2001; Götze, 2009).

Within quartz without significant Ti contents the 2.72 eV emission band is attributed to self-trapped excitons associated with oxygen vacancies (Gorton et al., 1997; Stevens-Kalceff and Phillips, 1995), or to an electron hole pair on an O vacancy and a peroxy linkage (Götze, 2009). Natural samples in our study contain different impurities and our data shows a strong positive correlation of the 2.72 eV peak intensity and the Ti content in quartz. These results may illustrate that either the 2.72 eV emission band is a composite band caused by overlapping of

313 the intrinsic emission with the band from Si-Ti substitution, or that titanium does not cause a
314 specific emission but distorts the crystal lattice, acting as an activator of the intrinsic emission.
315 Previously, Ti was also correlated with 2.6-2.8 eV (Sprunt, 1981) and 2.96 eV emission (Müller,
316 2000). The latter study found a linear correlation of the 2.96 eV emission intensity to the Ti
317 concentrations measured by EPMA, secondary ion mass spectrometry (SIMS) and laser
318 ablation inductively coupled plasma mass spectrometry (LA-ICP-MS). The Ti concentration also
319 correlates with the absorption intensity of the $[TiO_4/Li^+]^0$ center as determined by electron
320 paramagnetic resonance (EPR) spectroscopy (Müller, 2000), however, there is no direct
321 evidence for an association of this defect with the 2.96 eV emission.
322 The 2.05 eV CL peak can be attributed to intrinsic emission associated with a non-bridging
323 hydroxy precursor or radiation induced self-trapped exciton (Stevens-Kalceff and Phillips, 1995).
324 A CL band at around 2.1 eV is also commonly observed in cryptocrystalline and hydrothermal
325 quartz which might be related to very high concentrations of lattice defects like oxygen
326 vacancies, potentially due to processes of fast crystallization (Götze, 2009).
327 The 1.93 eV CL emission has previously been attributed to non-bridging oxygen hole center
328 defects (NBOHC), which are caused by unpaired electrons of oxygen atoms bonded to a
329 threefold coordinated silica atom (Stevens-Kalceff, 2009). High intensity of the 1.93 eV band is
330 common in volcanic and metamorphic quartz (Götze, 2009). Granitic quartz usually shows lower
331 1.93 eV intensity. Silanol groups are often considered to be precursors for these non-bridging
332 oxygen centers (Götze, 2009; Stevens-Kalceff and Phillips, 1995; Stevens-Kalceff, 2009).
333 Strained and broken O-Si bonds may also be responsible for the formation of the NBOHC,
334 which is common in metamorphic quartz (Götze, 2009; Stevens-Kalceff, 2009). Furthermore, O–
335 M bonds (with M being an alkali ion like Li^+, Na^+, etc.) can also be precursors for the 1.93 eV
336 emission (Stevens-Kalceff, 2009). Our results show that the 1.93 eV emission intensity is
337 negatively correlated with the aluminum concentration. Thus, we believe that the formation of
338 certain Al defects in quartz can quench the 1.93 eV emission. This could explain why published

data on correlation of Al with total CL emission is contradictory: if the 1.93 eV emission dominates (in our case in zones I, III, VI), fluctuations of the total emission will negatively correlate with Al concentrations, whereas if the 2.72 eV emission prevails over others the total emission will reflect fluctuations of Ti and there will be no correlation with aluminum. This is in good agreement with data from Rusk (2008) that high temperature quartz (high Ti concentration) shows a positive correlation between Al and CL intensity (total emission), whereas low temperature quartz (low Ti concentration) displays negative correlation of Al and total CL.

Although it is often assumed that Al/M^+ centers (with M^+ being a charge compensating cation, such as Li^+, Na^+) in quartz are associated with the ~3.2 eV emission band (Alonso et al., 1983; Luff and Townsend, 1990; Perny and Eberhardt, 1992), a band at ~3.2 eV was not detected in this study. Al substituting Si was also found correlating with the 2.79 eV emission (Müller, 2000), 2.9 eV emission (Ramseyer and Mullis, 1990) and 3.7 eV emission bands (Demars et al., 1996), but none of those bands was found associated with Al in our study.

Generally, radiation-induced electron-hole pairs in quartz can be temporarily trapped at oxygen ions adjacent to $Al\text{-}M^+$ centers forming $[AlO_4/M^+]^+$ centers. This can give rise to luminescence by trapping electrons and turning into $[AlO_4/M^+]^0$ centers. Above 200 K, however, the M^+ ion migrates easily, leaving behind $[AlO_4]^0$ centers at which recombination cannot occur and no luminescence is observed (Alonso et al., 1983). This could be the reason why a specific emission band associated with Al was not detected in our study. The scenario that Al occupies interstitial positions instead is less likely, as the strong negative correlation between Al content and 1.93 eV emission observed in our study is more consistent with substitutional incorporation of Al.

Botis and Pan (2009) investigated $[AlO_4/M^+]^0$ defects (where M^+ is a monovalent cation, e.g. H, Li, Na or K) in α-quartz by ab-initio calculations and concluded that 'incorporation of $[AlO_4/M^+]^0$ defects results in significant structural relaxations that extend at least to the nearest

Si atoms'. If high 1.93 eV intensity is caused by strained or broken O–Si bonds, substitution of Al and ensuing structural relaxation could result in a reduction in 1.93 eV emission. This would explain the strong negative correlation we observed between the 1.93 eV intensity and Al content (Fig 6d). If high 1.93 eV emission represents strained or broken O–Si bonds, this may also indicate more damage of the quartz lattice in those areas. If structural relaxation by $[AlO_4/M^+]^0$ formation reinforces the crystal lattice in high-Al areas, Al-poor areas would yield first on application of external stress, which could explain the occurrence of microfracture-networks in areas with high 1.93 eV emission, as can be seen in the marble-like texture of grain C in Figure 7.

In FT-IR, sharp absorption bands are generally attributed to well defined bonds, which are developed over isolated bonds and not affected by other bond vibrations, whereas broad bands are related to vibrations of molecules that affect one another (Müller, 2000). The 3378 and 3482 cm^{-1} peaks have previously been attributed to different OH species in quartz (Suzuki and Nakashima, 1999). The peak at 3378 cm^{-1} was found associated with three smaller broad peaks at 3205, 3317 and 3425 cm^{-1} and assigned to OH related to Al^{3+} that substitutes Si^{4+} atoms. The peak at 3482 cm^{-1} was assigned to Li-OH bond vibrations (Suzuki and Nakashima, 1999). The negative correlation we observed between the 1.93 eV CL intensity and 3378 cm^{-1} intensity (Fig 8) could imply that the 1.93 eV band is not related to Al-OH linkages, which supports the assumption that Al occurs predominantly in $[AlO_4/M^+]^0$ defects.

Trace element distribution: application to growth conditions

As discussed, Al distribution patterns are not always correlated with Ti distribution patterns within a single quartz grain. In many cases, Al shows gradual transitions between different zones where Ti displays sharp transitions. This difference in the character of the transitions can

be explained by the higher mobility of Al in quartz compared to Ti, making significant Al diffusion possible at lower temperatures (Cherniak et al., 2007).

Different distribution patterns for Ti and Al within quartz eyes can also indicate that different processes or conditions may control uptake of these elements. Substitution of Si by Ti is temperature dependent (Wark and Watson, 2006) and Ti incorporation in quartz increases with the crystallization temperature. Factors controlling Al content in quartz are not fully understood yet, neither are variations of Al content within a single quartz grain nor its relationship with Ti. Generally, the Al concentration in quartz increases during evolution of a melt: Al content is typically lower in quartz phenocrysts than in comb quartz, which is in turn lower compared to groundmass quartz (Breiter and Müller, 2009). Aluminum in hydrothermal quartz is believed to reflect its solubility in hydrothermal fluids, and to be strongly correlated with pH fluctuations (Rusk et al., 2008). It is also possible that Al variations in quartz result from changes in the growth rate. Al incorporation in quartz is a complex function of melt chemistry (e.g. availability of Al^{3+} and H^{+}, Li^{+} and Na^{+} in the melt, etc.) and physical conditions, such as temperature, pressure, and growth rates (Botis and Pan, 2009), but no data are available in the literature on what controls Al uptake specifically in magmatic quartz. Distribution of Al in quartz can also be determined by secondary processes such as diffusion and recrystallization of host quartz. It is impossible to conclude which particular conditions controlled Al uptake in our samples. It is apparent however, that those conditions changed repeatedly during quartz eye growth.

Sector and oscillatory zoning and clustering

Sector zoning is a common attribute of hydrothermal quartz, and is caused by different uptake of trace elements along different crystal faces (Müller, 2000; Rusk et al., 2008). It is commonly associated with disequilibrium growth (Ihinger and Zink, 2000). Different uptake of trace elements along different faces is usually explained by difference in a face's topography during hydrothermal growth, i.e. by different roughness of quartz faces: rougher faces absorb

more foreign ions than flat faces (Müller, 2000). The compositional differences between flat and rough faces usually decrease with increasing temperatures of crystallization and disappear at temperatures near the solidus, when all faces become rough and take up foreign ions in similar portions (Müller, 2000).

The development of sector zoning in other magmatic minerals is similarly attributed to kinetic factors and rapid changes in the crystallization conditions (Corfu et al., 2003). Watson and Liang (1995) proposed that the development of sector zoning depends on interrelation between growth rates and lattice diffusivity, and that there is a critical ratio of growth rate to lattice diffusivity of a certain component ‘above which the development of sector zoning is inevitable given surface-specific enrichment in this component'. As another example, Brophy et al. (1999) concluded that sector zoning in augite from high alumina basalts formed during augite supersaturation in magma due to rapid crystallization brought about by magma decompression and volatile exsolution.

Sector zoning in the studied samples occupies crystal cores, which show high OH^- and Li concentrations (FT-IR data, Fig 8), extremely low Ti content for magmatic quartz (10 - 30 ppm) and varying Al impurities (e.g. high Al in cluster R1 vs. low Al in cluster C), with patchy Al-poor zones. We believe that sector zoning in these quartz cores indicates their crystallization from an extremely fluid-rich melt under disequilibrium conditions. Absence of sector zoning in rims points to a change in crystallization conditions. Crystallization of the rims occurred from a melt depleted in Li and OH, which may infer that the fluid-rich phase had exsolved from the melt by that period. It is likely that during early stages of exsolution fluid was able to escape whereas during later stages, with increasing melt viscosity, fluid was trapped as primary inclusions in the latest quartz and as secondary inclusions in early quartz. This is in good agreement with the observed distribution of fluid inclusions: only the latest zone in cluster R2 (zone V) contains primary fluid inclusions.

Oscillatory zoning observed in all studied quartz grains is mostly determined by Ti variation and in some cases by Al (cluster C). Oscillatory zoning is believed to be an indicator of magmatic conditions (Müller, 2000; Wiebe et al., 2007), and is caused by a self-organized diffusion-controlled mechanism on the crystal-melt boundary layer (Müller, 2000).

Quartz crystals which are grouped in clusters show identical internal patterns with CL emission characteristics continuing from one grain to another (clusters R1 and C). Formation of clusters is common in magmatic systems, especially in porphyry systems (Vance, 1969; Wiebe et al., 2007). Preservation of clusters and identical CL patterns within them generally indicates that the attached grains crystallized together and were not disturbed after clustering; otherwise they would have been broken up and pulled apart. Thus, clustering of the quartz crystals prior to transport within a convecting magma is not likely.

Ti distribution, resorption textures, and application of the TitaniQ geothermometer

Our data show that adjacent quartz crystals within a single cluster often have different Ti concentrations (Fig 6a). Such uneven distribution of trace elements in quartz may indicate their uneven distribution in the melt, which may point to high growth rate conditions, when diffusion is too slow to provide an even distribution of elements. This may indicate non-equilibrium crystallization conditions.

Another major feature of the Ti distribution patterns are truncation textures, which are common in quartz from granitic and porphyritic intrusives (Müller et al., 2000; Wark et al., 2007; Wiebe et al., 2007). Truncation textures observed in the studied grains can imply that there was a resorption event postdating formation of low-Ti quartz cores and predating high-Ti quartz rim formation. Resorption in early magmatic quartz crystals can be caused by rapid, isothermal ascent of the magma into higher crust levels (Müller et al., 2000), whereas resorption of quartz cores during later magmatic stages can be related to rejuvenation of nearly solid crystal-mush (Wiebe et al., 2007).

463 Quartz eyes in porphyry environments are generally believed to crystallize within a
464 convecting magma in a magma chamber before its emplacement (Burnham and Ohmoto, 1980;
465 Cloos, 2001). However, it is commonly implied that the crystallinity of magma during
466 emplacement should not be more than 30% (Shinohara et al., 1995), otherwise it may be too
467 viscous to convect. Taking into account that magmas of intermediate composition are most
468 often associated with porphyry deposits, and that crystallization of quartz requires a high level of
469 silica saturation in magma, which is not commonly achieved until late stages of magma
470 evolution, we believe that quartz eyes in porphyry stocks crystallized late, after emplacement at
471 a subvolcanic level. Crystallization of quartz eyes in more felsic systems can start earlier and
472 continue until later stages after emplacement (Müller et al, 2000). Crystallization in-situ after
473 magma emplacement is in a good agreement with well-preserved clusters and the internal
474 patterns of quartz eyes (identical CL patterns in adjacent grains in a single cluster).

475 Although the observed patterns (truncation textures and high-Ti overgrowths) are generally
476 in good agreement with a rejuvenation scenario, it can also be caused by other processes. For
477 example, the same effect can be achieved if an increase in Ti activity occurs as a result of fluid
478 exsolution. In this case water, chlorine, alkali elements and some metals partition strongly into
479 the fluid phase, whereas Ti partitions strongly into the melt, thus increasing Ti activity in the
480 latter. Exsolution of a new phase will likely bring about disequilibrium between crystals, fluid and
481 melt phases, which will cause resorption of quartz crystals. When the equilibrium between
482 crystals, the exsolved fluid, and the residual melt is achieved, crystallization of quartz will
483 continue from the melt with higher Ti activity, and quartz overgrowths with higher Ti content will
484 form.

485 We applied the TitaniQ geothermometer (Wark and Watson, 2006) to estimate temperatures
486 of quartz crystallization (Table 2). The ranges of Ti content (provided by oscillatory zoning) in
487 cores (zones I, III, VI) and rims (II, IV, V and VII) were used for calculations and yielded a range
488 of crystallization temperatures (Table 2). Since Ti activities could not be precisely determined

and it is generally assumed that activity values lower than 0.5 are rare in silicic magmas (Wiebe et al., 2007), temperature ranges at a_{TiO2} = 0.5, 0.7 and 1 were calculated. If the Ti activity remained unchanged, then an increase in temperature of approximately 50-170°C was responsible for the increase in Ti uptake in cluster C with a corresponding increase of about 100-140°C in cluster R1. A 50-80°C increase would account for the change in Ti content from zone IV to V in cluster R2 (Table 2). The estimated range of crystallization temperatures for zone V is unreasonably high. Even the minimum temperatures (a_{TiO2} = 1) are in the range of 791-889°C, which appear to be too high for the late magmatic stage. This could indicate that above a certain concentration of around 150 ppm (Table 2), Ti not only substitutes Si but also occupies interstitial positions (Stevens-Kalceff, 2009) or occurs in nanoinclusions. In this case, the TitaniQ thermometer is inapplicable.

An increase in temperature alone without a decrease in water activity could cause resorption of quartz, but cannot be responsible for crystallization of new quartz. A reduction of a_{H2O} is needed to begin crystallization of new high temperature quartz (Wark et al., 2007; Wiebe et al., 2007). In several models a CO_2 fluid, which separated from the hot mafic magma injected underneath the pluton, triggered water separation and thus lowered a_{H2O} in the melt (Wark et al., 2007; Wiebe et al., 2007).

We believe, however, that in our case there is no need to invoke magma rejuvenation, as the increase in Ti uptake is more consistent with an increase in Ti activity due to fluid exsolution. An increase in Ti activity from 0.5 to 0.7 or to 1 can account for the changes in Ti uptake (Table 2). Moreover, it was shown that a_{TiO2} increases with decreasing pressure (Thomas et al., 2010). Hence, if fluid exsolution was triggered by a pressure drop then an abrupt increase in a_{TiO2} would be expected. Furthermore, CL patterns displaying dark cores overgrown by bright rims are common for plutonic quartz, especially in porphyry-related intrusions (Müller et al., 2010; Wiebe et al., 2007). Therefore, if hot mafic rejuvenation was responsible for formation of the observed patterns then CO_2-rich inclusions should be commonly trapped in quartz. However,

CO_2 inclusions in porphyry related plutons have been reported only rarely, and in the studied case CO_2 inclusions were not detected.

A temperature rise would enhance diffusion of Ti in quartz, which would make transitions between CL layers more gradual. Thus, sharp boundaries between both oscillatory and rim-core zones are also more consistent with the assumption that a_{TiO2} increased due to fluid exsolution rather than due to a temperature rise.

Crystallization of the quartz cores on the brink of the fluid exsolution is in good agreement with enrichment of cores in water, lithium and sometimes aluminum, and the presence of sector zoning. Accumulation of Al, Li and OH in the melt occurs during fractional crystallization. As a result of fluid exsolution a sharp decrease in OH and Li content in the melt occurs (Li, as chlorine-complexed element, partitions into the fluid phase), and thus their uptake in quartz is much lower. Aluminum is enriched in the melt phase, but its uptake in quartz is often controlled by OH or alkali element concentration in the melt (Müller et al., 2000) due to coupled substitution of Si by these compounds. Therefore, Al uptake in the quartz crystallized after the fluid exsolution can vary significantly.

Further accumulation of Al and Ti in the residual melt can bring about crystallization of extremely Al- and Ti-rich zones. In this case incorporation of Al and Ti in quartz can occur by both substituting Si atoms and trapping microinclusions. At this very late point of magma evolution the residual melt is too viscous for the fluid to escape and it is trapped as primary inclusions in the latest quartz and as secondary inclusions in the earlier phases. Zone V (cluster R2) is an example of such Ti-Al-rich quartz with primary fluid inclusions.

Summary on conditions of crystallization of quartz eyes

Crystallization of quartz eyes in porphyry environments is likely to begin after magma emplacement and on the brink of fluid exsolution. Quartz cores crystallize from the melt, which is extremely rich in Li and OH, and often show sector zoning. Subsequent exsolution of fluid

leads to disequilibrium between crystal, fluid and melt phases and also redistribution of elements between the fluid and the melt: OH and alkali metals together with chlorine and other volatiles partition into the fluid, whereas Ti tends to stay in the melt thus increasing the Ti activity of the melt. Sudden disequilibrium conditions cause dissolution of quartz crystals; after crystals-fluid-melt equilibrium is reached again the new high Ti quartz begins to crystallize.

Acknowledgements

This research was supported by a CODES Graduate Research Scholarship (University of Tasmania, grant №037923). We also thank Dr Thomas Rodemann (Central Science Laboratory) for support performing the FTIR analyses, and Murray Allan and Jens Götze for their comments that greatly improved the manuscript.

References

Allan, M.M., and Yardley, B.W.D. (2007) Tracking meteoric infiltration into a magmatic-hydrothermal system: a cathodoluminescence, oxygen isotope and trace element study of quartz from Mt. Leyshon, Australia. Chemical Geology, 240(3-4), 343–360.

Alonso, P.J., Halliburton, L.E., Kohnke, E.E., and Bossoli, R.B. (1983) X-Ray-induced luminescence in crystalline SiO_2. Journal of Applied Physics, 54(9), 5369-5375.

Ancey, M.F., Bastenaire, F., and Tixier, R. (1978) Application des méthodes statistiques en microanalyse. In F. Maurice, L. Meny, and R. Tixier, Eds., Microanalyse, microscopie électronique à balayage, Proceedings of Summer School, Sept. 11-16, St-Martin-d'Heres, France. Les Éditions du Physicien, Orsay, 323-347.

Botis, S.M., and Pan, Y.M. (2009) Theoretical calculations of $[AlO_4/M^+]^0$ defects in quartz and crystal-chemical controls on the uptake of Al. Mineralogical Magazine, 73(4), 537-550.

564 Breiter, K., and Müller, A. (2009) Evolution of rare-metal granitic magmas documented by
565 quartz chemistry. European Journal of Mineralogy, 21(2), 335-346.
566 Brophy, J.G., Whittington, C.S., and Park, Y.R. (1999) Sector-zoned augite megacrysts in
567 Aleutian high alumina basalts: implications for the conditions of basalt crystallization and
568 the generation of calc-alkaline series magmas. Contributions to Mineralogy and
569 Petrology, 135(2-3), 277-290.
570 Burnham, C.W., and Ohmoto, H. (1980) Late-stage processes of felsic magmatism. Mining
571 Geology Special Issue, 8, 1-11.
572 Cherniak, D.J., Watson, E.B., and Wark, D.A. (2007) Ti diffusion in quartz. Chemical Geology,
573 236, 65–74.
574 Cloos, M. (2001) Bubbling magma chambers, cupolas, and porphyry copper deposits.
575 International Geology Review, 43(4), 285-311.
576 Corfu, F., Hanchar, J.M., Hoskin, P.W.O., and Kinny, P. (2003) Atlas of zircon textures. Zircon,
577 53, 469-500.
578 D'Lemos, R.S., Kearsley, A.T., Pembroke, J.W., Watt, G.R., and Wright, P. (1997) Complex
579 quartz growth histories in granite revealed by scanning cathodoluminescence techniques.
580 Geology Magazine, 134(4), 549–552.
581 Demars, C., Pagel, M., Deloule, E., and Blanc, P. (1996) Cathodoluminescence of quartz from
582 sandstones: Interpretation of the UV range by determination of trace element
583 distributions and fluid-inclusion P-T-X properties in authigenic quartz. American
584 Mineralogist, 81(7-8), 891-901.
585 Gorton, N.T., Walker, G., and Burley, S.D. (1997) Experimental analysis of the composite blue
586 cathodoluminescence emission in quartz. Journal of Luminescence, 72-4, 669-671.

587 Götze, J., Plötze, M., and Habermann, D. (2001) Origin, spectral characteristics and practical
588 applications of the cathodoluminescence (CL) of quartz - a review. Mineralogy and
589 Petrology, 71, 225-250.
590 Götze, J., Plötze, M., and Trautmann, T. (2005) Structure and luminescence characteristics of
591 quartz from pegmatites. American Mineralogist, 90, 13-21.
592 Götze, J. (2009) Chemistry, textures and physical properties of quartz - geological interpretation
593 and technical application. Mineralogical Magazine, 73(4), 645-671.
594 Harrowfield, I.R., MacRae, C.M., and Wilson, N.C. (1993) Chemical imaging in electron
595 microprobes. 27th Annual MAS meeting 1993, p. 547-548. Microbeam Analysis Society.
596 Ihinger, P.D., and Zink, S.I. (2000) Determination of relative growth rates of natural quartz
597 crystals. Nature, 404(6780), 865-869.
598 Leeman, W.P., Vicenzi, E.P., MacRae, C.M.M., Wilson, N.C., Torpy, A., and Lee, C.-T.A.
599 (2008) Systematics of cathodoluminescence and trace element compositional zoning in
600 natural quartz from volcanic rocks: Ti mapping in quartz. Microscopy and Microanalysis,
601 14(Supplement S2).
602 Luff, B.J., and Townsend, P.D. (1990) Cathodoluminescence of synthetic quartz. Journal of
603 Physics-Condensed Matter, 2(40), 8089-8097.
604 MacRae, C.M., Wilson, N.C., Johnson, S.A., Phillips, P.L., and Otsuki, M. (2005) Hyperspectral
605 mapping - combining cathodoluminescence and X-ray collection in an electron
606 microprobe. Microscopy Research and Technique, 67(5), 271-277.
607 MacRae, C.M., and Wilson, N.C. (2007) Luminescence database I - minerals and materials.
608 Microscopy and Microanalysis, 14, p. 184-204

609 McGuire, A.V., Francis, C.A., and Dyar, M.D. (1992) Mineral standards for electron-microprobe
610 analysis of oxygen. American Mineralogist, 77(9-10), 1087-1091.
611 Monecke, T., Kempe, U., and Götze, J. (2002) Genetic significance of the trace element content
612 in metamorphic and hydrothermal quartz: a reconnaissance study. Earth and Planetary
613 Science Letters, 202, 709-724.
614 Müller, A. (2000) Cathodoluminescence and characterisation of defect structures in quartz with
615 applications to the study of granitic rocks, 228 p. Ph.D. thesis, Georg August University,
616 Göttingen, Germany.
617 Müller, A., Seltmann, R., and Behr, H.J. (2000) Application of cathodoluminescence to
618 magmatic quartz in a tin granite - case study from the Schellerhau Granite Complex,
619 Eastern Erzgebirge, Germany. Mineralium Deposita, 35, 169-189.
620 Müller, A., van den Kerkhof, A.M., Behr, H.J., Kronz, A., and Koch-Müller, M. (2010) The
621 evolution of late-Hercynian granites and rhyolites documented by quartz - a review. Earth
622 and Environmental Science Transactions of the Royal Society of Edinburgh, 100, 185-
623 204.
624 Nassau, K., and Prescott, B.E. (1975) Reinterpretation of smoky quartz. Physica Status Solidi a-
625 Applied Research, 29(2), 659-663.
626 Penniston-Dorland, S. (2001) Illumination of vein quartz textures in a porphyry copper ore
627 deposit using scanned cathodoluminescence: Grasberg Igneous Complex, Irian Jaya,
628 Indonesia. American Mineralogist, 86, 652–666.
629 Peppard, B.T., Steele, L.M., Davis, A.M., Wallace, P.J., and Anderson, A.T. (2001) Zoned
630 quartz phenocrysts from the rhyolitic Bishop Tuff. American Mineralogist, 86, 1034–
631 1052.

Perny, B., and Eberhardt, P. (1992) Microdistribution of Al, Li, and Na in α quartz: possible causes and correlation with short-lived cathodoluminescence. American Minerologist, 77, 534-544.

Ramseyer, K., and Mullis, J. (1990) Factors influencing short-lived blue cathodoluminescence of alpha-quartz. American Mineralogist, 75(7-8), 791-800.

Roedder, E. (1984) Fluid Inclusions. Reviews in Mineralogy, 12, 1-646.

Rusk, B.G., and Reed, M.H. (2002) Scanning electron microscope-cathodoluminescence analysis of quartz reveals complex growth histories in veins from the Butte porphyry copper deposit, Montana. Geology, 30(8), 727–730.

Rusk, B.G., Lowers, H.A., and Reed, M.H. (2008) Trace elements in hydrothermal quartz: Relationships to cathodoluminescent textures and insights into vein formation. Geology, 36(7), 547-550.

Shinohara, H., Kazahaya, K., and Lowenstern, J.B. (1995) Volatile transport in a convecting magma column: implications for porphyry Mo mineralization. Geology, 23(12), 1091-1094.

Sprunt, E.S. (1981) Causes of quartz cathodoluminescence colors. Scanning electron microscopy, p. 525-535, Chicago.

Stevens-Kalceff, M.A., and Phillips, M.R. (1995) Cathodoluminescence microcharacterization of the defect structure of quartz. Physical Review B, 52(5), 3122-3134.

Stevens-Kalceff, M.A. (2009) Cathodoluminescence microcharacterization of point defects in alpha-quartz. Mineralogical Magazine, 73(4), 585-605.

Suzuki, S., and Nakashima, S. (1999) In-situ IR measurements of OH species in quartz at high temperatures. Physics and Chemistry of Minerals, 26(3), 217-225.

Thomas, J.B., Watson, E.B., Spear, F.S., Shemella, P.T., Nayak, S.K., and Lanzirotti, A. (2010) TitaniQ under pressure: the effect of pressure and temperature on the solubility of Ti in quartz. Contributions to Mineralogy and Petrology, 160(5), 743-759.

Vance, J.A. (1969) On Synneusis. Contributions to Mineralogy and Petrology, 24(1), 7-29.

Vasyukova, O.V. (2011) Types and origin of quartz and quartz-hosted fluid inclusions in mineralised porphyries, 213 p. Ph.D. thesis, University of Tasmania, Hobart.

Wark, D.A., and Watson, E.B. (2006) TitaniQ: a titanium-in-quartz geothermometer. Contributions to Mineralogy and Petrology, 152, 743–754.

Wark, D.A., Spear, F.S., Cherniak, D.J., and Watson, E.B. (2007) Pre-eruption recharge of the Bishop magma system. Geology, 35(3), 235–238.

Watson, E.B., and Liang, Y. (1995) A simple model for sector zoning in slowly grown crystals: Implications for growth rate and lattice diffusion, with emphasis on accessory minerals in crustal rocks. American Mineralogist, 80(11-12), 1179-1187.

Watt, G.R., Wright, P., Galloway, S., and McLean, C. (1997) Cathodoluminescence and trace element zoning in quartz phenocrysts and xenocrysts. Geochimica et Cosmochimica Acta, 61(20), 4337-4348.

Wiebe, R.A., Wark, D.A., and Hawkins, D.P. (2007) Insights from quartz cathodoluminescence zoning into crystallization of the Vinalhaven granite, coastal Maine. Contributions to Mineralogy and Petrology, 154, 439-453.

Wilkinson, J.J. (2001) Fluid inclusions in hydrothermal ore deposits. Lithos, 55(1-4), 229-272.

Yang, B., Townsend, P.D., and Holgate, S.A. (1994) Cathodoluminescence and depth profiles of tin in float glass. Journal of Physics D: Applied Physics, 27(8), 1757-1762.

Captions

Figure 1

Ti calibration curve based on EPMA analyses: intensity of 2.72 eV peak vs. Ti (ppm) measured by EPMA.

Figure 2

Three principal Gaussian peaks centered at 1.93 eV, 2.05 eV, and 2.72 eV in cores (zones I, III, VI) and rims (zones II, IV, V, VII) of schematically shown cluster R1 (a), cluster R2 (b), cluster C (c). The light grey spectrum is the measured spectrum.

Figure 3

2.72 eV (a), 1.93 eV (b), and 2.05 eV (c) distribution maps and a trace element profile (d) for cluster R1. Zones I and II are labeled according to Fig 2a. Arrows in (a) - feldspar inclusions. Scale bars are 500 μm.

Figure 4

2.72 eV (a), 1.93 eV (b), 2.05 eV (c) distribution maps and a trace element profile (d) for cluster R2. Zones III, IV and V are labeled according to Fig 2b. Scale bars are 500 μm.

Figure 5

2.72 eV (a), 1.93 eV (b), and 2.05 eV (c) distribution maps and a trace element profile (d) for cluster C. Zones VI and VII are labeled according to Fig 2c. Rectangles in (b) are areas shown in Figure 6a, b, c. Note that two adjacent grains within the cluster show different 2.72 eV intensity (Ti concentrations) in outer zones (zones VIIa and VIIb).

Figure 6

Aluminum distribution vs the 1.93 eV intensity in cluster C. (a-c) - enlarged areas from Figure 5c showing 1.93 eV distribution, (d) - Al concentration plotted vs the 1.93 eV intensity. (e-g) - Al concentration profiles along lines shown in (a-c). Inserts in (e) are optical images showing the spots after EPMA which display spikes in Al concentration (arrows).

Figure 7

Distribution of fluid inclusions within quartz eyes. (a-c) - trails of secondary fluid inclusions in cluster C shown by arrows. (d-f) - zone V in cluster R2 with abundant very small fluid inclusions (1-2 μm). Note that there are only a few healed fractures, most inclusions seem to be primary. (a, d) - transmitted light, (b, e) - 2.72 eV map, (c, f) - 1.93 eV map. Arrows show healed fractures.

Figure 8

Infrared spectroscopy mapping, cluster R1. (a) - examples of IR spectra with peaks at 3482, 3425, 3378, 3317 and 3205 cm^{-1}. (b) - 1.93 eV map showing an area which was mapped by IR spectroscopy. (c) - 3482 cm^{-1} (Li-OH) map, (d) - 3378 cm^{-1} (Al-OH) map. Scale bars are 250 μm.

715 **Table 1 Characteristic features of quartz eyes and groundmass quartz in the studied samples**

Locality	Sample	Percentage of quartz eyes (%)	Quartz eye shapes	Quartz eye size (mm)	Groundmass quartz	Clusters	Number of grains studied
Rio Blanco	DC-DP-1	5-7	Euhedral, subhedral, anhedral (vitreous), rounded, amoeboid	0.5-5	fine grained	rare	17
	DC-DLP-1	10	Euhedral, subhedral, anhedral, rounded	0.5-3	fine grained	common	12
Climax	109647	3	Subhedral, anhedral, rounded	0.5-3	medium grained	abundant	14

716

717

718 **Table 2 Estimation of crystallization temperatures for the quartz grains R1, R2 and C based on**

719 **Ti-in-quartz geothermometer of Wark and Watson (2006)**

Grain	Zones (Fig 2)	Ti content range, ppm	Estimated crystallization temperatures, ^{o}C		
			Ti activity 0.5	Ti activity 0.7	Ti activity 1
R1	I	13-30	586-679	549-641	507-602
	II	42-72	719-788	679-744	639-700
R2	III	19-47	628-733	591-692	552-651
	IV	39-69	710-782	670-739	630-695
	V	147-287	893-1010	841-948	791-889
C	VI	10-44	546-724	506-684	455-644
	VII	40-67	713-778	673-735	633-692

720

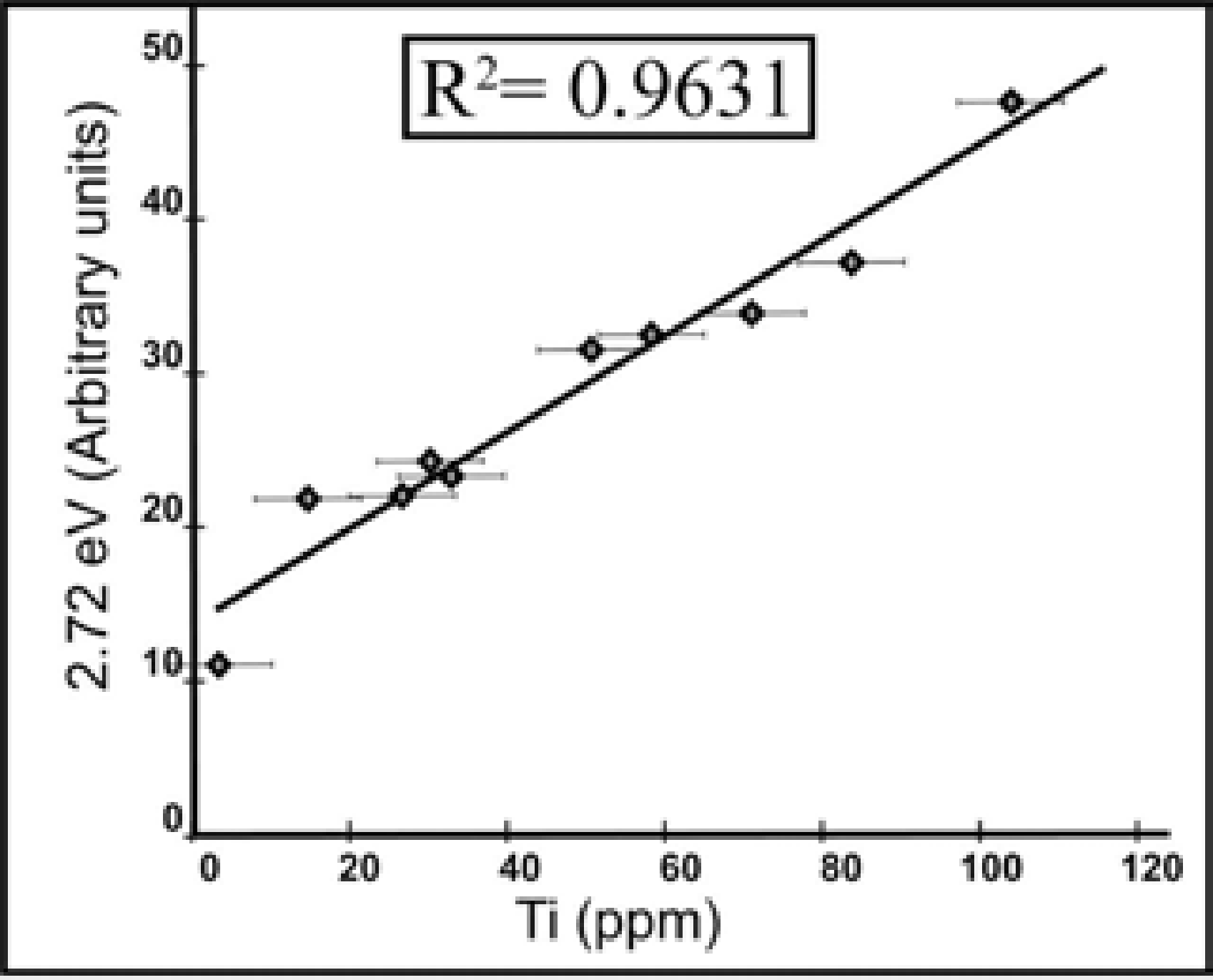

Figure 1 Ti calibration curve based on EPMA analyses: intensity of 2.72 eV peak vs. Ti (ppm) measured by EPMA.

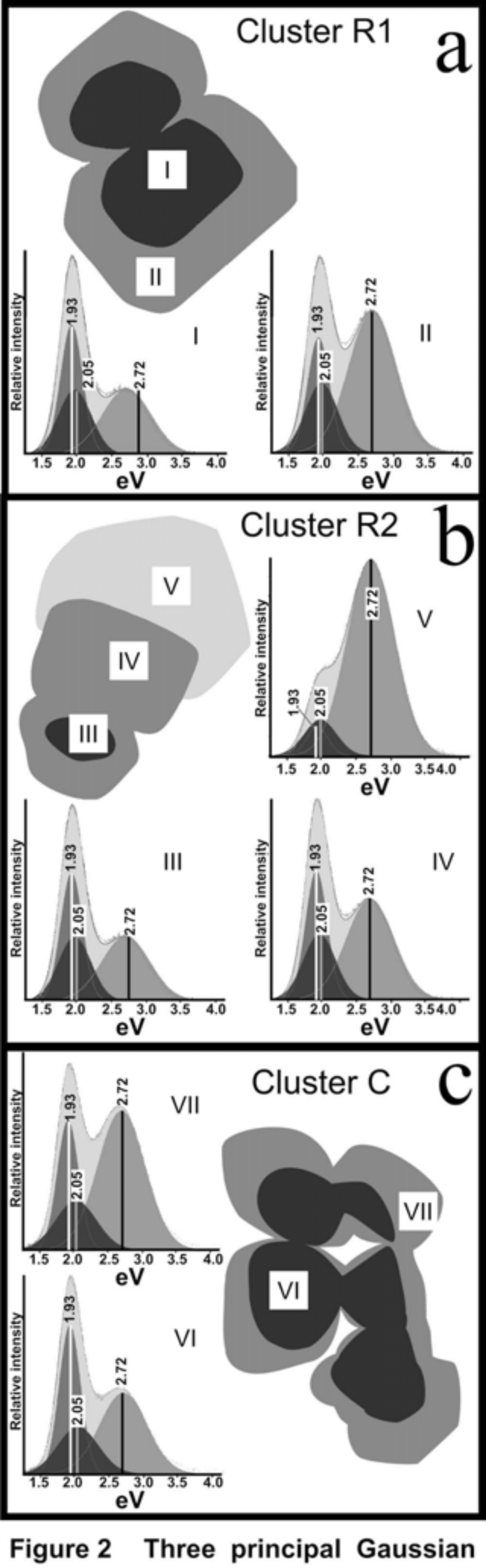

Figure 2 Three principal Gaussian peaks centered at 1.93 eV, 2.05 eV, and 2.72 eV in cores (I, III, VI) and rims (II, IV, V, VII) of schematically shown cluster R1 (a), cluster R2 (b), cluster C (c). The light grey spectrum is the measured spectrum.

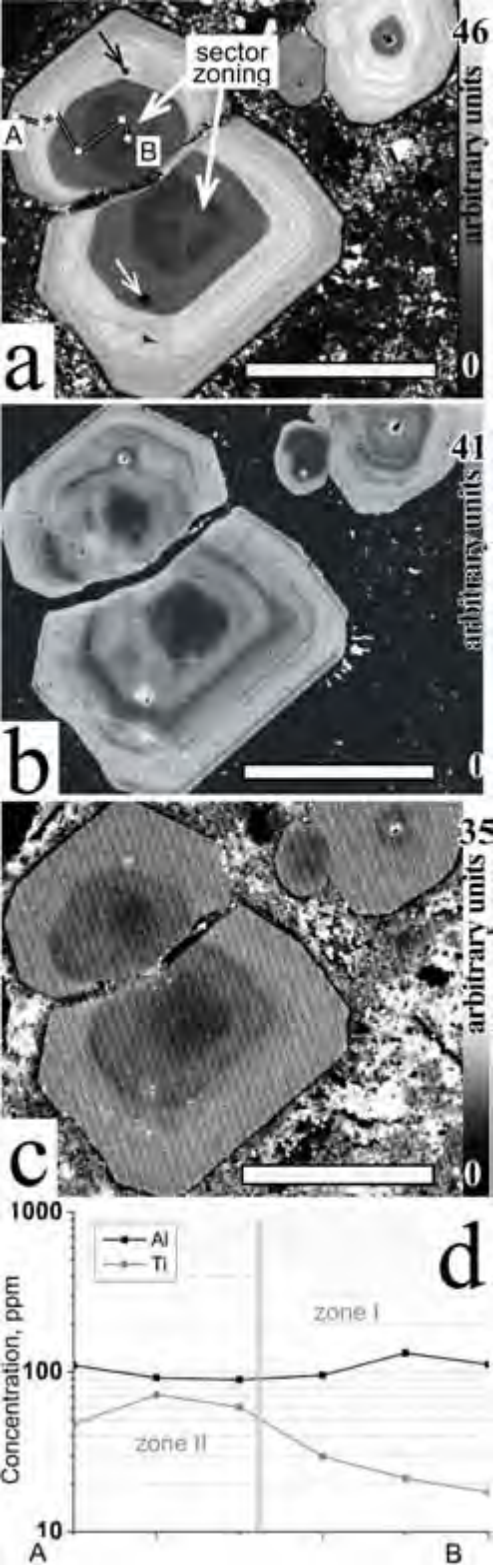
sector zoning
A
B
46
arbitrary units
0
a
41
arbitrary units
0
b
35
arbitrary units
0
c
1000
100
10
Concentration, ppm
Al
Ti
zone I
zone II
d
A
B

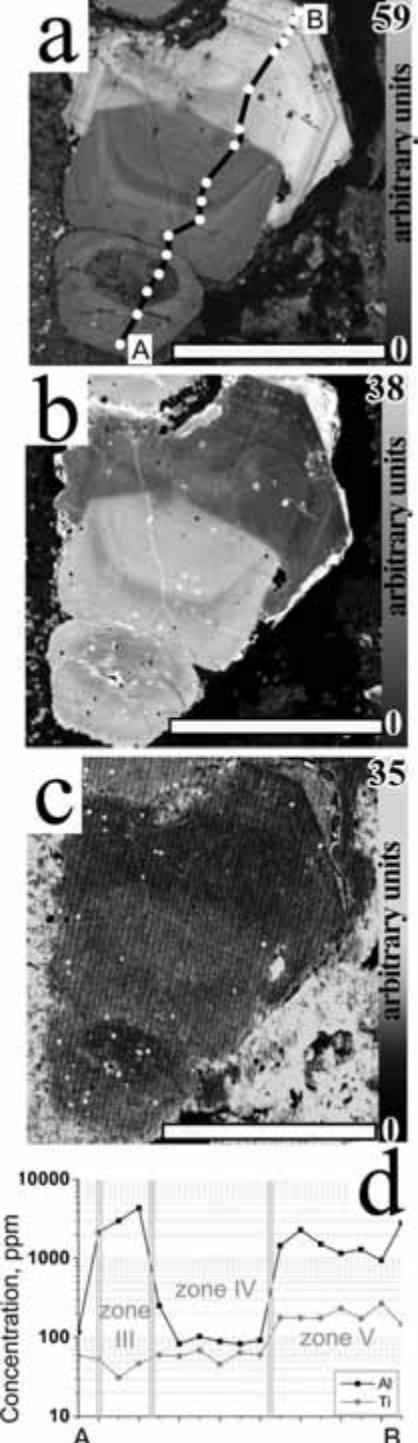
a
B
A
59
0
arbitrary units
b
38
0
arbitrary units
c
35
0
arbitrary units
d
10000
1000
100
10
Concentration, ppm
zone III
zone IV
zone V
Al
Ti
A
B

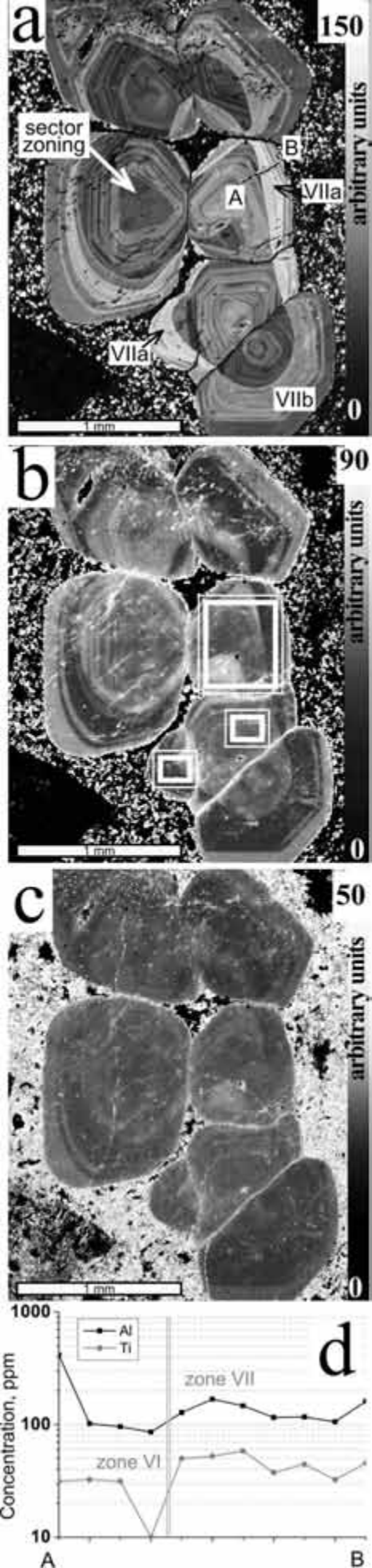
a
150
arbitrary units
0
sector zoning
B
A
VIIa
VIIa
VIIb
1 mm
b
90
arbitrary units
0
1 mm
c
50
arbitrary units
0
1 mm
d
1000
100
10
Concentration, ppm
Al
Ti
zone VII
zone VI
A
B

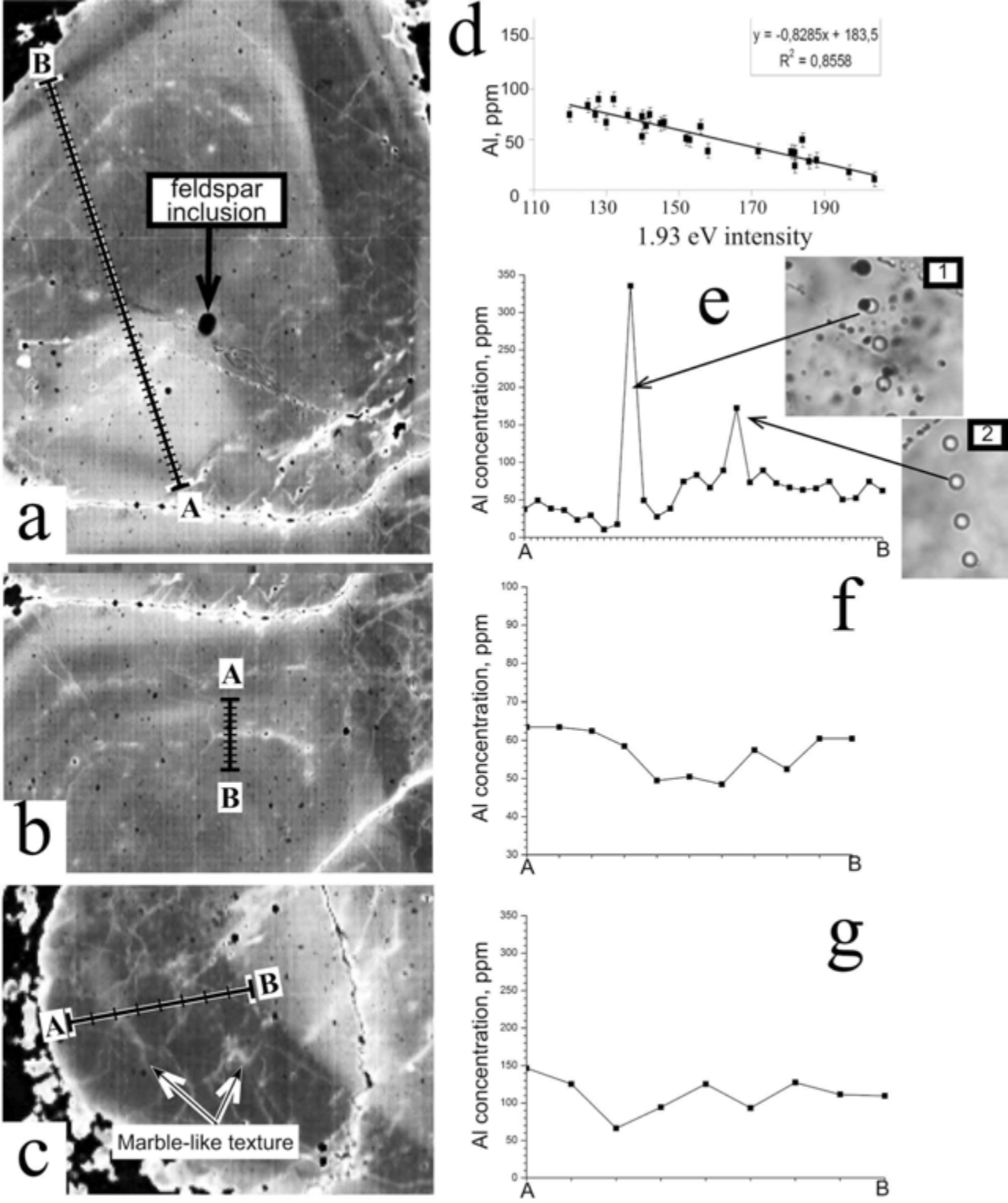

Figure 6 Aluminum distribution vs. the 1.93 eV intensity in cluster C. (a-c) - enlarged areas from Figure 5c showing 1.93 eV distribution, (d) - Al concentration plotted vs. the 1.93 eV intensity. (e-g) - Al concentration profiles along lines shown in (a-c). Inserts in (e) are optical images showing the spots after EPMA which display spikes in Al concentration (arrows).

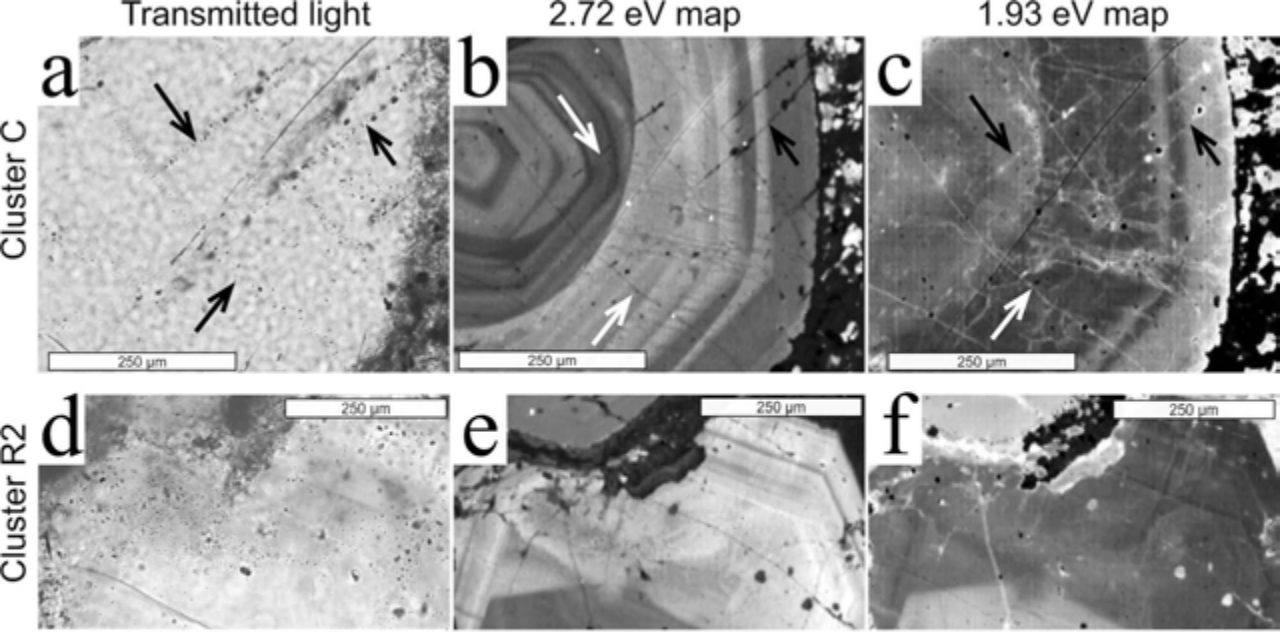

Figure 7 Distribution of fluid inclusions within quartz eyes. (a-c) - trails of secondary fluid inclusions in cluster C shown by arrows. (d-f) - zone V in cluster R2 with abundant very small fluid inclusions (1-2 µm). Note that there are only a few healed fractures, most inclusions seem to be primary. (a, d) - transmitted light, (b, e) - 2.72 eV map, (c, f) - 1.93 eV map. Arrows show healed fractures.

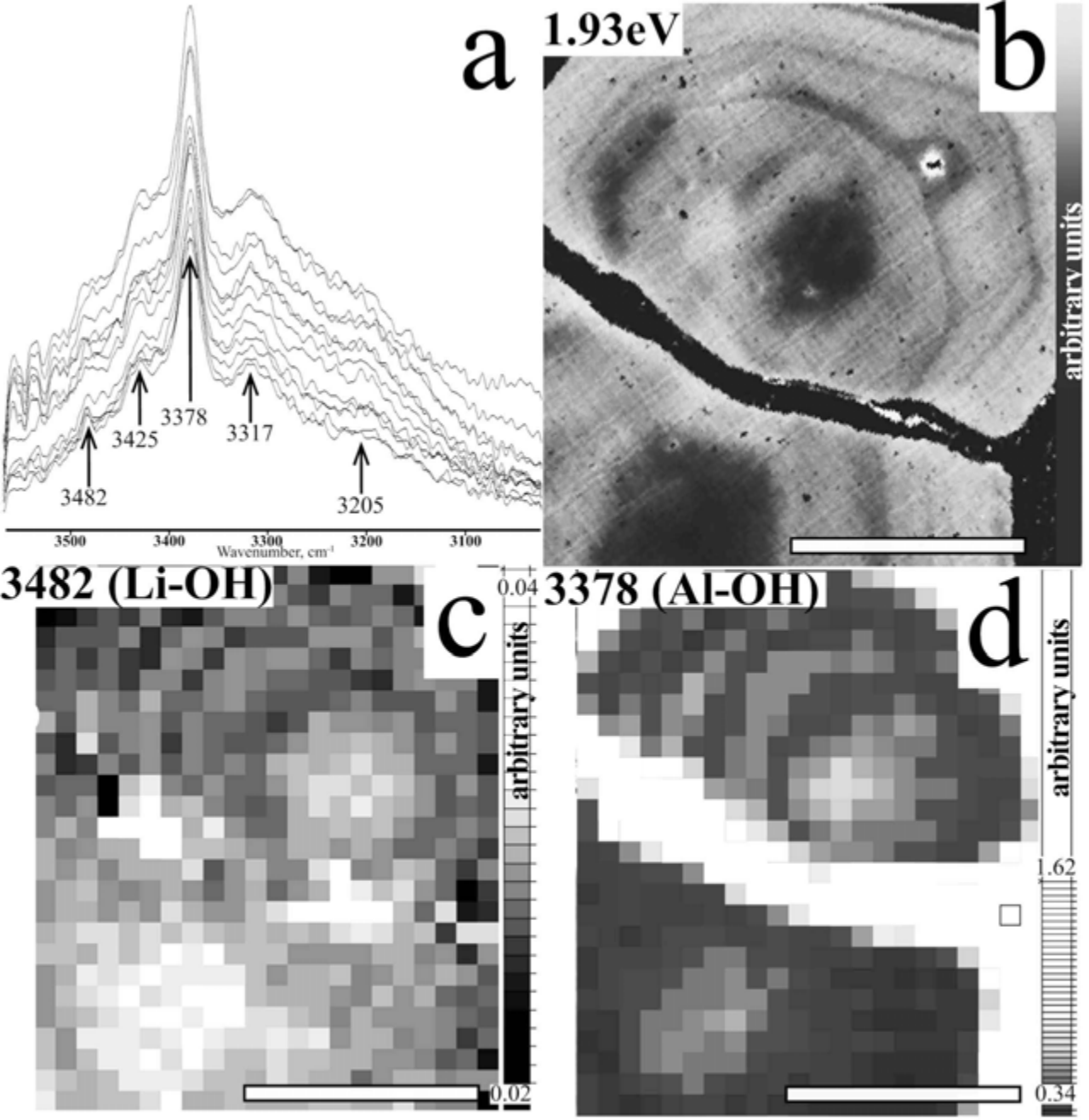

Figure 8 Infrared spectroscopy mapping, cluster R1. (a) - examples of IR spectra with peaks at 3482, 3425, 3378, 3317 and 3205 cm^{-1}. (b) - 1.93 eV map showing an area which was mapped by IR spectroscopy. (c) - 3482 cm^{-1} (Li-OH) map, (d) - 3378 cm^{-1} (Al-OH) map. Scale bars are 250 μm.